Effects of Active and Reactive Power Control on Inertia in DFIG-Based Wind Turbines

Xiang Guo, *Member, IEEE*, Qingbo Tang, Donghai Zhu, *Senior Member, IEEE*, Yini Zhou, *Student Member, IEEE*, Xudong Zou, *Member, IEEE*, Jiabing Hu, *Senior Member, IEEE*, and Yong Kang, *Fellow, IEEE*

***Abstract*—The inertia analysis for wind turbines (WTs) typically focuses on the electromechanical timescale. Active power control (APC) and phase-locked loop (PLL) are essential considerations while reactive power control (RPC) is often deemed negligible, particularly in stiff grid. However, such assumptions may be inappropriate. Therefore, this article aims to comprehensively examine the effects of APC and RPC on the inertia for doubly fed induction generator-based WTs. Firstly, phase motion models are developed by incorporating various combinations of control loops, including APC, RPC, and different PLL configurations. Subsequently, the impacts of the APC and RPC on the inertia are examined in detail. The analysis reveals that the APC diminishes inertia, whereas the RPC significantly enhances the inertia. Additionally, special attention should be given to phase characteristics of the inertia transfer function, as they can substantially influence inertial performance. Furthermore, an improved frequency support method is proposed, which achieves superior frequency response without necessitating the PLL bandwidth to be adjusted to extremely low values, such as 1 Hz or lower. Finally, the analysis and the proposed method are validated through experiments.**

***Index Terms*—Active power control (APC), doubly fed induction generator (DFIG), inertia control, reactive power control (RPC), wind turbine.**

NOMENCLATURE

$P_{\rm e}$, $Q_{\rm e}$	Active and reactive power.
$V_{\rm s}$, $\Psi_{\rm s}$	Stator voltage and stator flux.
$E_{\rm m}$	Excitation voltage.
$I_{\rm s}$, $I_{\rm r}$	Stator current and rotor current.
$\delta_{\rm E}$	Internal rotor angle between excitation voltage vector $\mathbf{E_m}$ and stator voltage vector $\mathbf{V_s}$.
$R_{\rm s}$	Stator resistance.
X_s, $X_{\rm m}$	Stator reactance and mutual reactance.
$L_{\rm s}$, $L_{\rm r}$, $L_{\rm m}$	Stator, rotor, and magnetizing inductance.
$\theta_{\rm pll}$, $\theta_{\rm ctrl}$	PLL phase angle and power control angle.
$\theta_{\rm E}$, $\theta_{\rm s}$	Phase angle of excitation voltage vector $\mathbf{E_m}$ and stator voltage vector $\mathbf{V_s}$.
$k_{\rm ppll}$, $k_{\rm ipll}$	Proportional and integral coefficients of the PLL controller.
$\omega_{-3{\rm dB}}$, $\zeta_{\rm pll}$	PLL bandwidth and damping coefficient.
ω_1	Rated grid angular frequency.
$J(s)$	Inertia transfer function.
$T_{\rm pll}$, $T_{\rm f}$	Filter time constant of PLL and LPF.
$I_{\rm P}$, $P_{\rm P}$	Desired d-axis rotor current change and active power change under frequency excursion.

Subscripts

d, q	*Direct and quadrature-axis components.*
s, r	Stator and rotor side.
0	Initial steady value before disturbance. Bold case variable denotes instantaneous space phasor.

Received 18 November 2024; revised 11 March 2025; accepted 25 April 2025. Date of publication 9 May 2025; date of current version 30 June 2025. This work was supported in part by the National Natural Science Foundation of China under Grant 52407228 and in part by the State Key Laboratory of Advanced Electromagnetic Technology under Grant AET 2024KF003. Recommended for publication by Associate Editor D. Oliveira. *(Corresponding author: Donghai Zhu.)*

Xiang Guo is with the School of Electrical Engineering, China University of Mining and Technology, Xuzhou 221116, China (e-mail: guoxiang@cumt.edu.cn).

Qingbo Tang is with the Hubei Key Laboratory of Marine Electromagnetic Detection and Control, Wuhan 430064, China (e-mail: m201771393@alumni.hust.edu.cn).

Donghai Zhu, Yini Zhou, Xudong Zou, Jiabing Hu, and Yong Kang are with the State Key Laboratory of Advanced Electromagnetic Technology, School of Electrical and Electronic Engineering, Huazhong University of Science and Technology, Wuhan 430074, China (e-mail: zhudh@hust.edu.cn; zhouyn@hust.edu.cn; xdzou@mail.hust.edu.cn; j.hu@hust.edu.cn; ykang@hust.edu.cn).

Color versions of one or more figures in this article are available at https://doi.org/10.1109/TPEL.2025.3568206.

Digital Object Identifier 10.1109/TPEL.2025.3568206

I. INTRODUCTION

IN RECENT years, the power system has transitioned from fossil fuel-based generation to renewable power generation (RPG) [1], [2]. While the large-scale integration of renewable energy contributes to environmental and societal benefits, it also introduces challenges that make the power system more vulnerable [3]. Specifically, voltage and frequency excursions have become more significant under contingency situations, raising concerns among transmission system operators (TSOs) [4].

To ensure grid security, TSOs have mandated that RPG equipment should comply with grid codes, which include requirements for voltage support, inertia control, and primary frequency regulation capabilities [5], [6]. Against this background, grid-forming (GFM) control has gained widespread applications, particularly with increasing wind power penetrations. A key advantage of GFM-based wind turbines (WTs) is their ability to emulate the external characteristics of synchronous generators (SGs), thereby facilitating inertial response [7]. In contrast, the grid-following (GFL)-based WTs under typical parameter

configurations are generally unable to provide inertial response. To address this limitation, additional frequency-related control loops are integrated into the outer loop to modify the output active power of WTs. This capability is often referred to as virtual, emulated, artificial, or synthetic inertia [8].

The doubly fed induction generator (DFIG)-based WT gets scaled applications in wind power plants (WPPs). Traditionally, it is assumed that DFIG-based WTs do not provide an inertial response during frequency disturbances because they operate at the maximum power point or their rotor is decoupled from the grid. [9], [10], [11]. This perspective primarily considers aerodynamic operating features and structural topologies. However, this may be incomplete, as it overlooks the influence of hierarchical control loops—including the power control loop, current control loop, and phase-locked loop (PLL) on the inertial response of DFIG-based WTs.

For the inertia analysis of WTs, active power control (APC) is typically considered due to its influence at the initial stages of frequency disturbances [12]. However, the impact of the phase-locked loop (PLL) remains a subject of debate, particularly concerning its bandwidth, which ranges from a few Hertz to tens of Hertz. When the PLL bandwidth is set to tens of Hertz, DFIG-based WTs may not exhibit an inertial response, rendering the PLL's impact on power dynamics negligible [13]. This does not imply that an inertial response is unattainable but suggests that the inertial response is concealed under high PLL bandwidth settings. To release the hidden inertia, extensive research has been conducted to explore the inertial provision mechanisms of DFIG-based WTs. For instance, researchers have established phase motion models that consider the coupling between APC and PLL, demonstrating that a noticeable inertial response can be achieved by reducing the PLL bandwidth to extremely low values, typically below 1 Hz or even as low as 0.1 Hz [14], [15]. Further investigations have explored the impacts of APC in DFIG-based WTs with low PLL bandwidths, indicating that the control parameters of APC have limited influences on inertia [16]. These findings confirm that the PLL significantly affects the inertial response. Subsequently, Guo et al. [17] reconceptualized the PLL by analogies to the phase motion model of SGs and led to the proposal of various methods for optimizing the PLL to enhance the inertial response [18], [19], [20]. It appears that, in inertia analysis, the focus is often on the electromechanical timescale, with APC and PLL being inherently included in the modeling, and has been progressively deepened in academic research. However, such integration may not be entirely appropriate, as the impacts of APC and PLL cannot be fully explained in isolation. Notably, the influence of APC on inertia is seldom examined in depth.

The reactive power control (RPC) is often overlooked, particularly in a stiff grid [21], where active power and reactive power are typically decoupled. Even in weak grid conditions, although active and reactive power are coupled during dynamic processes, the control parameters of the voltage controller have a minor impact on the inertia of DFIG-based WTs with constant terminal voltage control [16]. [22] found that negative inertia can occur when reactive power operating points are set unreasonably for WTs with adjustable reactive power control. However, the effects of RPC on inertia and the extent of its influence remain unclear.

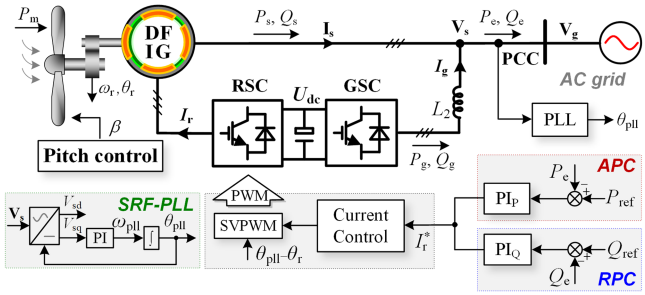

Fig. 1. Diagram of the DFIG-based WT system.

Targeting these issues, this article aims to comprehensively examine the effects of APC and RPC on the inertia for DFIG-based WTs. The major contributions are as follows:

1) The significance of the magnitude and phase characteristics of the inertia transfer function is demonstrated for DFIG-based WTs, which is achieved through the phase motion model that incorporates the PLL. And, the analysis results indicate that the conclusions obtained in synchronous reference frame (SRF)-PLL on inertia are applicable to other types of PLLs.
2) The conventional understanding that APC must be considered while RPC can be neglected in inertia analysis for DFIG-based WTs is challenged. By comparing cases with and without considering APC and RPC, it is found that APC diminishes inertia, whereas RPC significantly enhances inertia.
3) Based on the theoretical analysis, an improved frequency support method is proposed. This proposed method achieves superior inertia performance compared to traditional methods that require tuning the PLL bandwidth below 1 Hz. More importantly, the PLL bandwidth for the proposed method does not need to be adjusted to extremely low values.

The rest of the article is organized as follows: Section II gives the system description and introduces the typical phase motion model. Section III presents phase motion models that consider various types of PLLs and illustrate the significance of bode diagram for the inertia transfer function. Section IV examines the impacts of APC and PLL on inertia and further proposes a frequency support method. The correctness of the analysis is verified by the experiments in Section V. Finally, Section VI concludes this article.

II. System Description and Typical Phase Motion Model for DFIG-Based WTs

A. System Description

Fig. 1 shows the diagram of the DFIG-based WT system. The DFIG-based WT is connected to the public grid via the back-to-back converters, namely rotor-side converter (RSC) and grid-side converter (GSC). The GSC can be ignored as most mechanical power is transferred through the stator side,

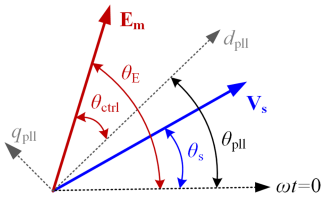

Fig. 2. Vector diagram for DFIG-based WTs during frequency disturbances.

as performed in [15], [19]. The RSC control usually adopts a dual control loop for superior performance. The APC and RPC are employed for achieving the d-axis and q-axis rotor current, respectively. The active power reference is obtained from the power tracking curve. The control targets of RPC normally include terminal voltage and reactive power, but the latter is more common in practice [23], [24]. The current control ensures high-quality current but can be ignored in this article because the article mainly focuses on electromechanical dynamics. The SRF-PLL provides the phase foundation for the RSC control system through the stator voltage orientation.

B. Typical Phase Motion Mode By Considering APC and PLL

The basic dynamic model of the stator side for the DFIG-based WT in the synchronous reference frame by adopting the generator and motor convention at the stator and rotor side can be expressed as follows [30]:

$$\begin{cases} \mathbf{V_s} = -R_{\rm s}\mathbf{I_s} + d\mathbf{\Psi_s}/dt + j\omega_1\mathbf{\Psi_s} \\ \mathbf{\Psi_s} = -L_{\rm s}\mathbf{I_s} + L_{\rm m}\mathbf{I_r} \end{cases} \tag{1}$$

$$P_e = V_{\rm sd}I_{\rm sd} + V_{\rm sq}I_{\rm sq}. \tag{2}$$

The inertial response of the DFIG-based WT is generally up to several seconds and belongs to the electromechanical timescale. The APC and RPC are usually included in the mechanical timescale. The PLL can be catalogized to both the electromagnetic timescale and electromechanical timescale, which is determined by the PLL bandwidth. The current control usually affects the dynamic around 0.01 s and belongs to the electromagnetic timescale, which can pose little impact on the electromechanical dynamic. Therefore, the electromagnetic dynamic is normally neglected in the field of inertial analysis, as in [14], [19].

Except for ignoring the flux dynamic, the stator resistance can also be disregarded for the power loss on the stator resistance is very small. Then, the stator voltage equation in (1) can be expressed as follows:

$$\mathbf{V_s} = j\omega_1\mathbf{\Psi_s} = -j\omega_1 L_{\rm s}\mathbf{I_s} + j\omega_1 L_{\rm m}\mathbf{I_r}. \tag{3}$$

Define the excitation vector $\mathbf{E_m}$ of the DFIG-based WT as follows:

$$\mathbf{E_m} = j\omega_1 L_{\mathbf{m}}\mathbf{I_r} = jX_{\mathbf{m}}\mathbf{I_r} = E_{\mathbf{md}} + jE_{\mathbf{mq}}. \tag{4}$$

Then, the active power $P_{\rm e}$ in (2) can be re-expressed as follows:

$$P_{\rm e} = E_{\rm m}V_{\rm s}\sin(\delta_{\rm E})/X_{\rm s}. \tag{5}$$

Fig. 2 shows the vector diagram of DFIG-based WTs in the synchronous reference frame during the frequency disturbances. Based on Fig. 2, the internal rotor angle $\delta_{\rm E}$ can be expressed as follows:

$$\delta_{\rm E} = \theta_{\rm E} - \theta_{\rm s} = \theta_{\rm ctrl} + \theta_{\rm pll} - \theta_{\rm s}. \tag{6}$$

According to (5) and (6), the small-signal expression of active power $\Delta P_{\rm e}$ can be expressed as follows:

$$\begin{aligned} \Delta P_{\rm e} = & \underbrace{\frac{V_{\rm s0}}{X_{\rm s}}\sin(\delta_{\rm E0})\Delta E_{\rm m}}_{\text{intertal voltage amplitude}} + \underbrace{\frac{E_{\rm m0}V_{\rm s0}}{X_{\rm s}}\cos(\delta_{\rm E0})\Delta\delta_{\rm E}}_{\text{intertal voltage phase}} \\ & + \underbrace{\frac{E_{\rm s0}}{X_{\rm s}}\sin(\delta_{\rm E0})\Delta V_{\rm s}}_{\text{terminal voltage amplitude}} = \frac{V_{\rm s0}}{X_{\rm s}}\sin(\delta_{\rm E0})\Delta E_{\rm m} \\ & + k_\delta\Delta\delta_{\rm E} + k_{\rm Vs}\Delta V_{\rm s}. \end{aligned} \tag{7}$$

$\Delta V_{\rm s}$ and $\Delta E_{\rm md}$ can be neglected since the terminal voltage and corresponding control hardly affect the active power dynamics in stiff grid. Then, according to (4) and Fig. 2, $\Delta E_{\rm m}$ can be expressed as follows:

$$\begin{aligned} \Delta E_{\rm m} &= \frac{E_{\rm md0}}{\sqrt{E_{\rm md0}^2 + E_{\rm mq0}^2}}\Delta E_{\rm md} + \frac{E_{\rm mq0}}{\sqrt{E_{\rm md0}^2 + E_{\rm mq0}^2}}\Delta E_{\rm mq} \\ &\approx \frac{E_{\rm mq0}}{E_{\rm m0}}\Delta E_{\rm mq} \end{aligned} \tag{8}$$

$$\Delta\theta_{\rm ctrl} = \frac{E_{\rm md0}}{E_{\rm m0}^2}\Delta E_{\rm mq} - \frac{E_{\rm mq0}}{E_{\rm m0}^2}\Delta E_{\rm md} \approx k_{\rm cmq}\Delta E_{\rm mq}. \tag{9}$$

Taking (8) and (9) into (7), (10) can be obtained

$$\begin{aligned} \Delta P_{\rm e} &\approx \underbrace{\frac{V_{\rm s0}}{X_{\rm s}}\sin(\delta_{\rm E0})\frac{E_{\rm mq0}}{E_{\rm m0}}}_{k_{\rm PEq}}\Delta E_{\rm mq} + k_\delta\left(\Delta\theta_{\rm ctrl} + \Delta\theta_{\rm pll} - \Delta\theta_{\rm s}\right) \\ &= k_{\rm PEq}\Delta E_{\rm mq} + k_\delta\left(k_{\rm cmq}\Delta E_{\rm mq} + \Delta\theta_{\rm pll} - \Delta\theta_{\rm s}\right). \end{aligned} \tag{10}$$

The transfer function of SRF-PLL $G_{\rm pll}(s)$ reflects the relation between $\Delta\theta_{\rm s}$ and $\Delta\theta_{\rm pll}$ and can be expressed as follows:

$$G_{\rm pll}(s) = \frac{\Delta\theta_{\rm pll}(s)}{\Delta\theta_{\rm s}(s)} = \frac{k_{\rm ppll}s + k_{\rm ipll}}{s^2 + k_{\rm ppll}s + k_{\rm ipll}}. \tag{11}$$

Combined with the control block of RSC in Fig. 1, (4), (6), (8), (9), (10) and (11), the small-signal model of the DFIG-based WT in the electromechanical timescale can be obtained, as shown in Fig. 3(a).

Furthermore, by block transformation, Fig. 3(b) can be achieved. The coefficient $k_{\rm Eq}$ in Fig. 3(b) equals

$$k_{\rm Eq} = k_{\rm cmq} + k_{\rm PEq}/k_\delta = 1/E_{\rm md0}. \tag{12}$$

The final phase motion model by considering the APC and PLL is shown in Fig. 3(c) and the inertia transfer function $J_{\rm APC}(s)$ can be derived as follows:

$$J_{\rm APC}(s) = \frac{\omega_1 k_\delta\left(1 - G_{\rm pll}(s)\right)}{s^2\left(G_{\rm pll}(s) + k_\delta X_{\rm m}k_{\rm Eq}G_{\rm piP}(s)\right)}. \tag{13}$$

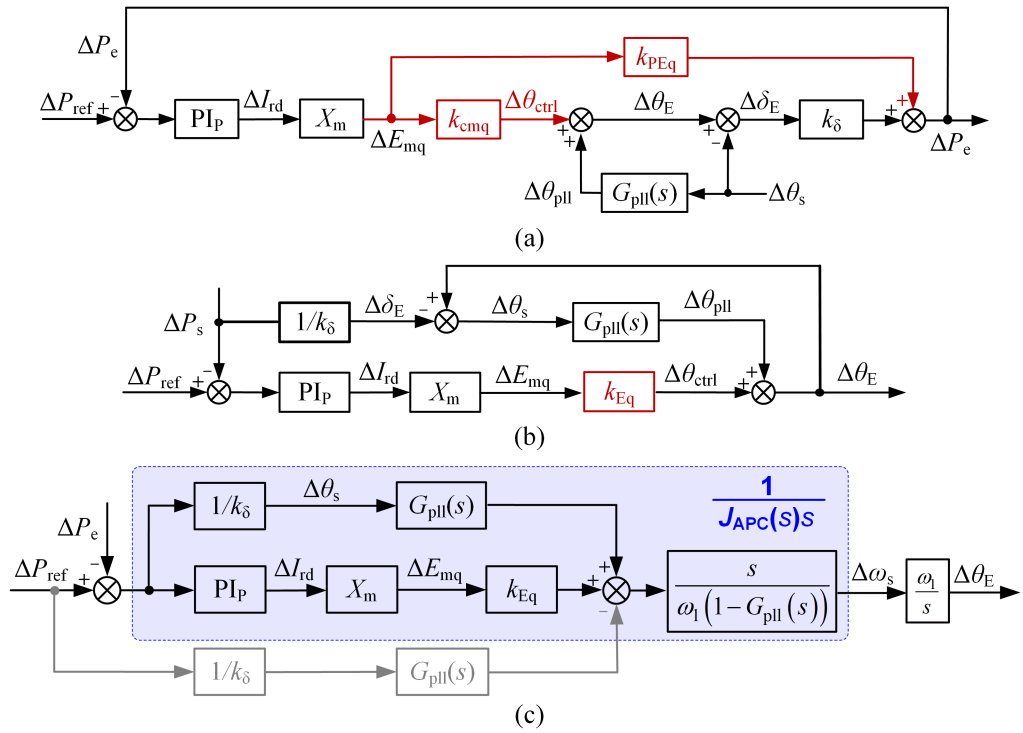

Fig. 3. Model for DFIG-based WTs in the electromechanical timescale. (a) Active power dynamic model under power imbalance. (b) Simplification process. (c) Pphase motion model by considering the APC and PLL.

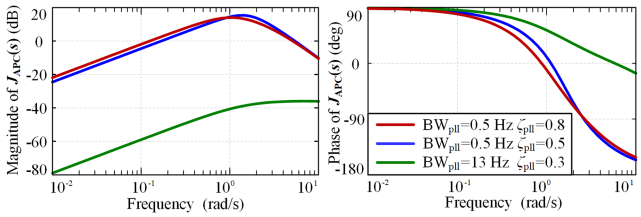

Fig. 4. Bode diagram of the inertia transfer function $J_{\mathrm{APC}}(s)$ under the typical phase motion model of DFIG-based WTs.

Based on (13), it can be inferred that the inertia of the DFIG-based WT is primarily affected by the PLL and APC parameters. As demonstrated in [16], the PLL shows a greater impact on inertia than the APC. Fig. 4 shows different PLL parameter configurations on the inertia for DFIG-based WTs. As can be seen, the DFIG-based WT presents no inertia under high PLL bandwidth ($\mathrm{BW_{pll}}$) whereas low PLL bandwidth benefits for inertia provision. Besides, the PLL damping coefficient (ζ_{pll}) has limited influences on the inertia. Actually, similar conclusions have been explained in detail in [14]. The reason for reintroducing Fig. 4 in this article is to highlight the magnitude and phase change trend of the inertia transfer function. Two critical points can be observed in Fig. 4.

1) The magnitude in the range of 10^{-2}–10^{0} rad/s is a straight line with a slope of 20dB/decade.
2) The phase decreases from 90° and finally stables at −180°.

In summary, existing research on the typical phase motion model, which considers the couplings between the APC and PLL, primarily focuses on the magnitude characteristics to assess the impacts of control parameters on inertia. However, the significance of phase characteristics for the inertia transfer function is rarely addressed. Furthermore, most studies analyze the inertia of DFIG-based WTs by considering all control loops collectively, without examining the individual impact of each control loop on inertia.

III. Significance of Bode Diagram for Inertia Transfer Function and Impacts of PLLs on Inertia

The significance of the bode diagram for the inertia transfer function, especially the phase diagram, has not been demonstrated. This section aims to address this gap by the established phase motion model, focusing solely on the PLL, and exploring the impact of different types of PLLs on inertia.

A. Phase Motion Model By Sorely Considering the PLL

When the APC is disregarded, the power dynamic model in Fig. 3(a) can be re-expressed as in Fig. 5(a), where the feedback loop for the electromagnetic power (P_{e}) and the active power controller no longer exist. Additionally, the input of the model in Fig. 3(a) shifts from the mechanical power reference (P_{ref}) to the d-axis rotor current reference ($I_{\mathrm{rd}}{}^{*}$) in Fig. 5(a). The d-axis rotor current reference is calculated by dividing the mechanical power reference by the coefficient k_{P}, based on the steady-state model of DFIG-based WT.

Fig. 5(b) illustrates the simplification process of the power dynamic model. As shown, two control loops determine the phase dynamic of the internal voltage $\mathbf{E_m}$. The mechanical power loop reflects the inherent power property of the DFIG-based WT and

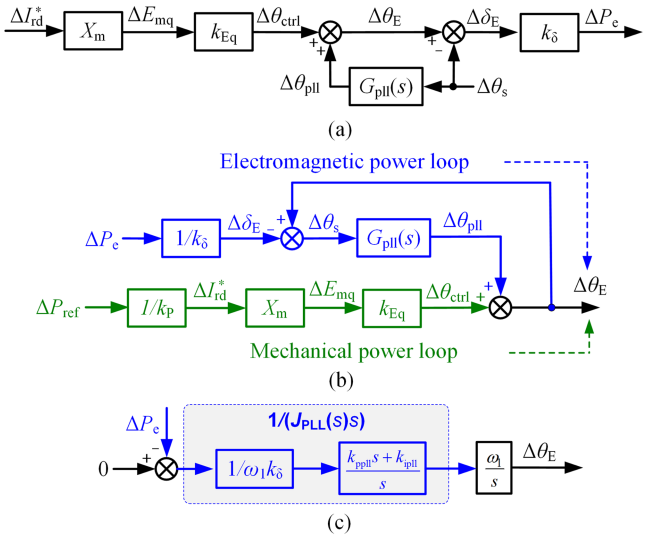

Fig. 5. Model for DFIG-based WTs by sorely considering the SRF-PLL. (a) Power dynamic model for DFIG-based WTs. (b) Simplification process. (c) Phase motion model by considering SRF-PLL.

decides the steady-state phase angle θ_{E} of $\mathbf{E_m}$. Notably, no controllers are included in this loop. The electromagnetic power loop primarily reflects the dynamic process of phase angle θ_{E} for $\mathbf{E_m}$. And, the PLL controller parameters, along with the control structures, have many configurations. Since this article focuses on the power dynamics induced by the converter control, the mechanical power is assumed to remain constant during the frequency disturbances [15]. In other words, the small signals of the mechanical power ΔP_{ref} and the control angle $\Delta\theta_{\mathrm{ctrl}}$ equal 0. Then, Fig. 5(c) can be easily obtained. And, the inertia transfer function $J_{\mathrm{pll}}(s)$ by sorely considering the PLL can be expressed as follows:

$$J_{\mathrm{PLL}}(s) = \frac{\omega_1 k_\delta (1 - G_{\mathrm{pll}}(s))}{s^2 G_{\mathrm{pll}}(s)} = \frac{\omega_1 k_\delta}{k_{\mathrm{ppll}} s + k_{\mathrm{ipll}}} = \frac{\omega_1 k_\delta}{k_{\mathrm{ipll}}} \frac{1}{(k_{\mathrm{ppll}}/k_{\mathrm{ipll}})\, s + 1} = \frac{\omega_1 k_\delta}{k_{\mathrm{ipll}}} \frac{1}{T_{\mathrm{pll}} s + 1}. \quad (14)$$

According to (14), it can be seen that the inertia of DFIG-based WTs when sorely considering the PLL is a first-order transfer function. And, the gain of the inertia transfer function is $\omega_1 k_\delta / k_{\mathrm{ipll}}$, which is determined by the operation point and the integral coefficient k_{ipll} of the PI controller in the PLL.

B. Significance of Bode Diagram for Inertia Transfer Function

The SRF-PLL is usually designed according to the bandwidth and damping coefficient. And, the detailed expressions for the proportional coefficient k_{ppll} and integral coefficient k_{ipll} in the SRF-PLL are given in [25] and listed as follows:

$$k_{\mathrm{ppll}} = \frac{2\xi_{\mathrm{pll}}\omega_{-3dB}}{\sqrt{1 + 2\xi_{\mathrm{pll}}^2 + \sqrt{4\xi_{\mathrm{pll}}^4 + 4\xi_{\mathrm{pll}}^2 + 2}}} \quad (15)$$

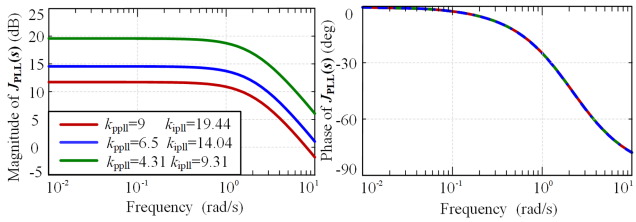

Fig. 6. Significance of the magnitude of the inertia transfer function $J_{\mathrm{pll}}(s)$.

TABLE I
PLL PARAMETERS WITH THE SAME T_{pll}

k_{ppll}	k_{ipll}	T_{pll}	$\mathrm{BW}_{\mathrm{pll}}$	ζ_{pll}
4.31	9.31		1.0	0.707
6.5	14.04	**0.46**	1.36	0.8674
9	19.44		1.76	1.02

The bold value used for emphasis and they mainly mean the bold value of the three cases.

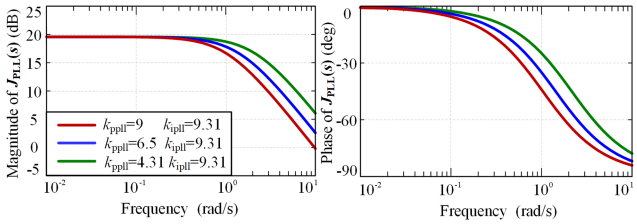

Fig. 7. Significance of the phase of the inertia transfer function $J_{\mathrm{pll}}(s)$.

$$k_{\mathrm{ipll}} = \frac{\omega_{-3dB}^2}{1 + 2\xi_{\mathrm{pll}}^2 + \sqrt{4\xi_{\mathrm{pll}}^4 + 4\xi_{\mathrm{pll}}^2 + 2}}. \quad (16)$$

The inertia analysis puts more emphasis on the integral coefficient k_{ipll} and filter time constant T_{pll}, as seen in (14). In contrast, the design guidance of the PLL focuses more on the bandwidth and damping, based on (15) and (16). Clearly, the design guidance and the inertia analysis for the PLL are fundamentally different. Therefore, the following analysis will provide all the parameters for the SRF-PLL.

Fig. 6 intends to illustrate the significance of the magnitude of inertia transfer function by maintaining the phase constant. The magnitude of the inertia transfer function determines the power boost during the inertial response. A larger magnitude usually corresponds to a more significant inertial response, which has been confirmed by many researchers and will not be further discussed here. Fig. 6 also shows the impacts of the integral coefficient k_{ipll} on the inertia with the filter time constant $T_{\mathrm{pll}} = 0.46$. As observed, the phase characteristics are completely uniform, varying from 0° to −90°. The maximum magnitude in the bode diagram increases from 12 to 19 dB as the integral coefficient of the PLL decreases from 19.44 to 9.31. From the perspective of the PLL design guidance, it can be concluded that a low PLL bandwidth $\mathrm{BW}_{\mathrm{pll}}$ and a smaller damping coefficient ζ_{pll} contribute to a better inertial response according to Table I, in line with the analysis in [19].

TABLE II
PLL PARAMETERS WITH THE SAME k_{ipll}

k_{ppll}	k_{ipll}	T_{pll}	$\mathrm{BW}_{\mathrm{pll}}$	ζ_{pll}
4.31		0.46	1.0	0.707
6.5	**9.31**	0.7	1.25	1.06
9		0.97	1.6	1.47

The bold value used for emphasis and they mainly mean the bold value of the three cases.

Fig. 7 intends to illustrate the significance of the phase of the inertia transfer function by maintaining the magnitude as constant as possible. The magnitude characteristics remain almost constant in the range of 10^{-2}–10^{0} rad/s but show slight variations in the range of 10^{0}–10^{1} rad/s. A lower phase delay in the bode diagram generally contributes to a faster inertial response [14], Therefore, the phase of the inertia transfer function directly affects the response speed of the inertial response. Fig. 7 also shows the impacts of the filter time constant T_{pll} on the inertia with the integral coefficient $k_{\mathrm{ipl}} = 9.31$. As shown, the phase reduces as T_{pll} increases. And, a smaller filter time constant T_{pll} (or a smaller proportional coefficient k_{ppll}) brings in faster inertial response performances. From the perspective of the PLL design guidance, similar conclusions obtained in Fig. 6 can also be drawn from Table II.

C. Impacts of Different Types of PLL on Inertia

The above analysis uses the SRF-PLL as an example to illustrate the impact of the PLL on inertia. Since it is challenging to verify whether these conclusions hold for all types of PLLs, this article focuses on commonly used PLLs, including the low-pass filter (LPF)-SRF-PLL, decoupled double synchronous reference frame PLL (DDSRF-PLL), and dual second-order generalized integrator PLL (DSOGI-PLL), to validate the findings. The structures of these three PLL types are shown in Fig. 8.

The LPF-SRF-PLL introduces the LPF to attenuate the harmonics. The overall small-signal model for LPF-SRF-PLL is similar to the SRF-PLL and is shown in Fig. 9.

Based on Fig. 9, the transfer function $G_{\mathrm{LPF\text{-}SRF\text{-}PLL}}(s)$ of the LPF-SRF-PLL can be derived as follows:

$$G_{\mathrm{LPF-SRF-PLL}}(s) = \frac{k_{\mathrm{ppll}}s + k_{\mathrm{ipll}}}{T_f s^3 + s^2 + k_{\mathrm{ppll}}s + k_{\mathrm{ipll}}}. \quad (17)$$

Taking (17) into (14), (18) can be obtained

$$J_{\mathrm{LPF-SRF-PLL}}(s) = \omega_1 k_\delta \frac{T_f s + 1}{k_{\mathrm{ppll}}s + k_{\mathrm{ipll}}}. \quad (18)$$

Based on (18), the bode diagram of the inertia transfer function for DFIG-based WTs with LPF-SRF-PLL under different filter constants can be achieved, as shown in Fig. 10. The control parameters of the PI controller for the LPF-SRF-PLL are also selected as $k_{\mathrm{ppll}} = 4.31$ and $k_{\mathrm{ipll}} = 9.31$. The value of T_{f} is typically lower than 0.05 to ensure the response speed of PLL Note that the LPF-SRF-PLL reverts to the SRF-PLL when $T_{\mathrm{f}} = 0$. As can be seen in Fig. 10, the impacts of the filter constant T_{f} is most prominent in the range of 10^{1}–10^{2} rad/s. However, for the inertia analysis of the DFIG-based WT, the scope of concern in the bode diagram is typically below 10^{1} rad/s. Therefore, the filter constant T_{f} may have minimal impact on the inertia when considering the range of value for T_{f} and frequency range of interest for inertia analysis. The impacts of PI control parameters in the LPF-SRF-PLL are similar to those in the SRF-PLL and will not be further discussed.

The DDSRF-PLL shown in Fig. 8(b) is usually used in the situation of the grid with unbalanced voltage. Since the decoupling network eliminates the effects of the negative-sequence

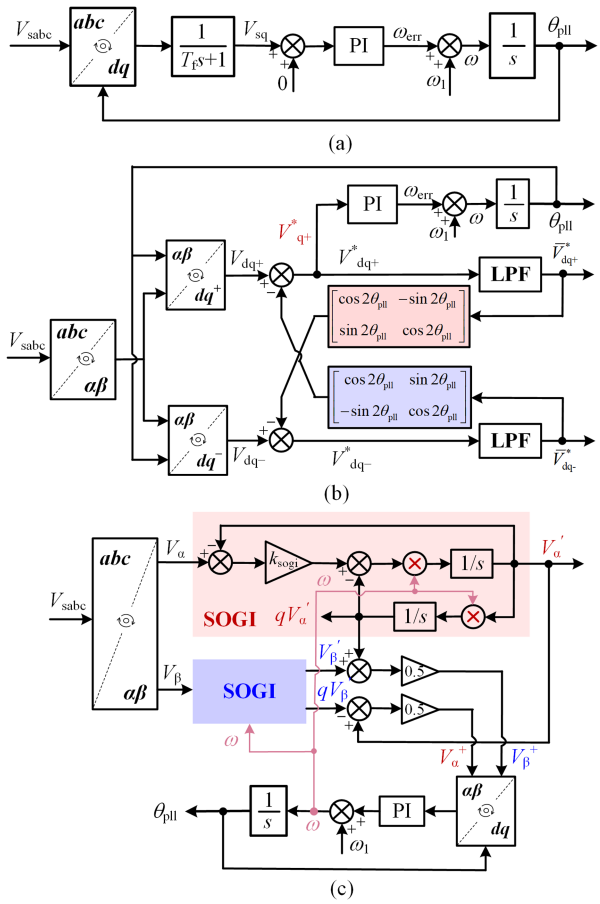

Fig. 8. Structures of commonly used PLLs in DFIG-based WTs. (a) LPF-SRF-PLL. (b) DDSRF-PLL. (c) DSOGI-PLL.

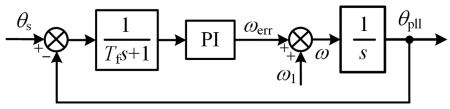

Fig. 9. Small-signal model of the LPF-SRF-PLL.

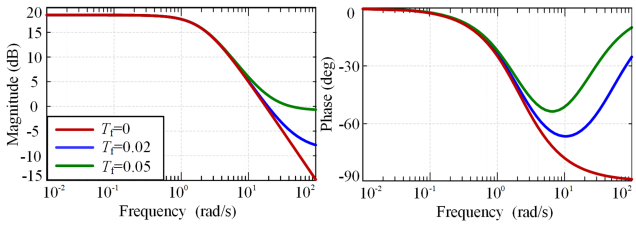

Fig. 10. Bode diagram of inertia transfer function $J_{\mathrm{LPF\text{-}SRF\text{-}PLL}}(s)$ for DFIG-based WTs with LPF-SRF-PLL.

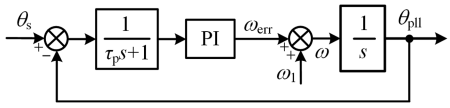

Fig. 11. Small-signal model of DSOGI-PLL.

component, the small-signal model for the DDSRF-PLL is the same as the SRF-PLL. The detailed derivation of the small-signal model for the DDSRF-PLL can be referred to [26]. Therefore, the impacts of the DDSRF-PLL on the inertia are the same as the SRF-PLL.

The DSOGI-PLL shown in Fig. 8(c) gets wide attention due to its advantages of frequency adaptive performance, low computational burden, and satisfied dynamic performance. A detailed derivation of the small-signal model for DSOGI-PLL, as depicted in Fig. 11, can be referred to [27]. And, τ_{p} is the time constant and can be expressed as follows:

$$\tau_{\mathrm{p}} = \frac{2}{k_{\mathrm{sogi}}\omega_1} \tag{19}$$

where k_{sogi} is the gain factor of the second-order generalized integrator.

Comparing Fig. 11 with Fig. 9, it can be found that the small-signal model of the DSOGI-PLL is similar to the LPF-SRF-PLL. Therefore, the inertia characteristics of the DFIG-based WT with DSOGI-PLL can also be analyzed by the LPF-SRF-PLL.

Based on the analysis above, it can be concluded that the inertia characteristics of DFIG-based WTs with commonly used PLLs, such as SRF-PLL, LPF-SRF-PLL, DDSRF-PLL, and DSOGI-PLL, can be analyzed using either SRF-PLL or LPF-SRF-PLL. Additionally, the filter constant T_{f} in the LPF-SRF-PLL has minimal impact on the inertia characteristics of DFIG-based WTs. Therefore, the inertia characteristics of the DFIG-based WT with commonly used PLLs all can be analyzed by the SRF-PLL. From this perspective, the conclusions drawn from SRF-PLL hold for commonly used PLLs in the DFIG-based WT.

IV. Impacts of APC and RPC on Inertia and Improved Frequency Support Method for DFIG

The APC is usually included in inertia analysis while the RPC is often ignored. This is because active power and reactive power are usually decoupled in stiff grid and the reactive power has little impact on the dynamic of the active power. However, this does not imply that the RPC is irrelevant to the inertia analysis. The impacts of both the APC and RPC will be discussed in this section.

A. Phase Motion Model By Considering the RPC and PLL

The reactive power Q_{e} for the DFIG-based WT can be expressed as follows [28]:

$$Q_{\mathrm{e}} = \frac{E_{\mathrm{m}}V_{\mathrm{s}}\cos\left(\theta_{\mathrm{E}}-\theta_{\mathrm{s}}\right)}{X_{\mathrm{s}}} - \frac{V_{\mathrm{s}}^2}{X_{\mathrm{s}}} = \frac{E_{\mathrm{m}}V_{\mathrm{s}}\cos\left(\delta_{\mathrm{E}}\right)}{X_{\mathrm{s}}} - \frac{V_{\mathrm{s}}^2}{X_{\mathrm{s}}}. \tag{20}$$

When considering the impacts of the RPC, the small-signal expression for (8) and (9) should be re-expressed as follows:

$$\Delta E_{\mathrm{m}} = \frac{E_{\mathrm{md0}}}{E_{\mathrm{m0}}}\Delta E_{\mathrm{md}} + \frac{E_{\mathrm{mq0}}}{E_{\mathrm{m0}}}\Delta E_{\mathrm{mq}} \tag{21}$$

$$\begin{aligned}\Delta\theta_{\mathrm{ctrl}} &= \frac{E_{\mathrm{md0}}}{E_{\mathrm{m0}}^2}\Delta E_{\mathrm{mq}} - \frac{E_{\mathrm{mq0}}}{E_{\mathrm{m0}}^2}\Delta E_{\mathrm{md}} \\ &= k_{\mathrm{cmq}}\Delta E_{\mathrm{mq}} - k_{\mathrm{cmd}}\Delta E_{\mathrm{md}}.\end{aligned} \tag{22}$$

According to (7) and (21), the small-signal expression for the active power P_{e} can be derived as follows:

$$\begin{aligned}\Delta P_{\mathrm{e}} &= \frac{V_{\mathrm{s0}}}{X_{\mathrm{s}}}\sin\left(\delta_{\mathrm{E0}}\right)\left(\frac{E_{\mathrm{md0}}}{E_{\mathrm{m0}}}\Delta E_{\mathrm{md}} + \frac{E_{\mathrm{mq0}}}{E_{\mathrm{m0}}}\Delta E_{\mathrm{mq}}\right) \\ &\quad + \frac{E_{\mathrm{m0}}V_{\mathrm{s0}}}{X_{\mathrm{s}}}\cos\left(\delta_{\mathrm{E0}}\right)\Delta\delta_{\mathrm{E}} + \frac{E_{\mathrm{s0}}}{X_{\mathrm{s}}}\sin\left(\delta_{\mathrm{E0}}\right)\Delta V_{\mathrm{s}} \\ &\approx k_{\mathrm{PEd}}\Delta E_{\mathrm{md}} + k_{\mathrm{PEq}}\Delta E_{\mathrm{mq}} + k_{\delta}\Delta\delta_{\mathrm{E}}.\end{aligned} \tag{23}$$

Different from the small-signal expressions in [14] and [19], the term $k_{\mathrm{cmd}}\Delta E_{\mathrm{md}}$ in (22) and the term $k_{\mathrm{PEd}}\Delta E_{\mathrm{md}}$ in (23) are not ignored as they will reflect the impacts of the RPC on the dynamic of active power P_{e} during the frequency disturbances.

Based on (20) and (21), the small-signal expression for the reactive power can be derived as follows:

$$\begin{aligned}\Delta Q_{\mathrm{e}} &= \frac{V_{\mathrm{s0}}\cos\left(\theta_{\mathrm{E0}}-\theta_{\mathrm{s0}}\right)}{X_{\mathrm{s}}}\Delta E_{\mathrm{m}} + \frac{E_{\mathrm{m0}}\cos\left(\theta_{\mathrm{E0}}-\theta_{\mathrm{s0}}\right)}{X_{\mathrm{s}}}\Delta V_{\mathrm{s}} \\ &\quad - \frac{E_{\mathrm{m0}}V_{\mathrm{s0}}\sin\left(\theta_{\mathrm{E0}}-\theta_{\mathrm{s0}}\right)}{X_{\mathrm{s}}}\left(\Delta\theta_{\mathrm{E}}-\Delta\theta_{\mathrm{s}}\right) - \frac{2V_{\mathrm{s0}}}{X_{\mathrm{s}}}\Delta V_{\mathrm{s}} \\ &\approx \underbrace{\frac{V_{\mathrm{s0}}\cos\left(\theta_{\mathrm{E0}}-\theta_{\mathrm{s0}}\right)}{X_{\mathrm{s}}}\frac{E_{\mathrm{md0}}}{E_{\mathrm{m0}}}}_{k_{\mathrm{Emd}}}\Delta E_{\mathrm{md}} \\ &\quad + \underbrace{\frac{V_{\mathrm{s0}}\cos\left(\theta_{\mathrm{E0}}-\theta_{\mathrm{s0}}\right)}{X_{\mathrm{s}}}\frac{E_{\mathrm{mq0}}}{E_{\mathrm{m0}}}}_{k_{\mathrm{Emq}}}\Delta E_{\mathrm{mq}} \\ &\quad - k_{\mathrm{q}}\left(\Delta\theta_{\mathrm{E}}-\Delta\theta_{\mathrm{s}}\right).\end{aligned} \tag{24}$$

Combining (11), (12), (21), (22), (23), (24) with Fig. 3(a), Fig. 12(a) can be obtained. As can be seen, compared with Fig. 3(a) and Fig. 5(a), the APC is neglected while the RPC is emphasized in Fig. 12(a). And, the manner to achieve the d-axis rotor current reference is the same as in Fig. 5(b).

The mechanical power P_{ref} in Fig. 12(a) is also considered to be constant, as in Fig. 5(c). Further, ΔP_{ref} equals 0 and Fig. 12(b) can be obtained by block transformation. It is re-emphasized that the electromagnetic power dynamic in this article arises from the inherent converter control effect, rather than introducing other control loops. And, the transfer function $G_{\mathrm{q}}(s)$ in Fig. 12(b) can be expressed as follows:

$$G_{\mathrm{q}}\left(s\right) = -\frac{X_{\mathrm{m}}G_{\mathrm{piQ}}\left(s\right)}{1-k_{\mathrm{Emd}}X_{\mathrm{m}}G_{\mathrm{piQ}}\left(s\right)}. \tag{25}$$

Afterward, by expanding the term $k_{\mathrm{q}}G_{\mathrm{q}}(s)$ into loops 1, 2, and 3 in Fig. 12(b) and integrating these loops, Fig. 12(c) can be easily achieved. And, the relationship between ΔP_{e} and $\Delta\theta_{\mathrm{E}}$

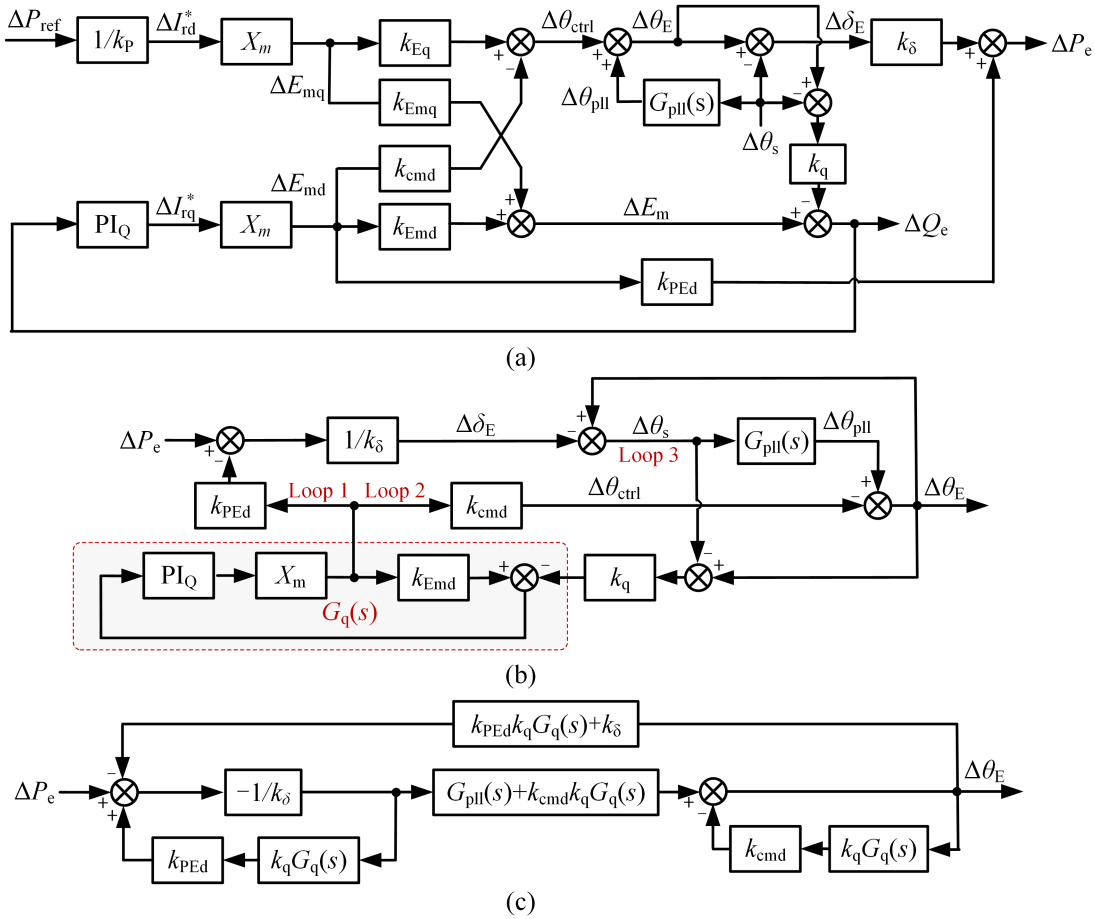

Fig. 12. Phase motion model when considering the RPC and PLL. (a) Power dynamic model for DFIG-based WTs. (b) Simplification process. (c) Simplified phase motion model.

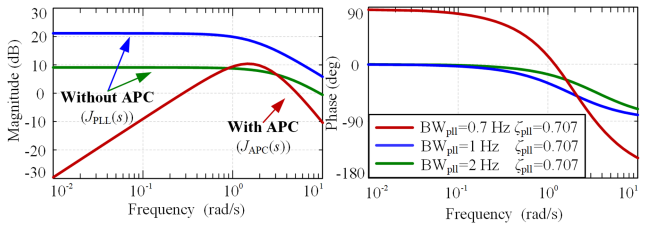

Fig. 13. Bode diagram of inertia transfer function $J_{\mathrm{pll}}(s)$ and $J_{\mathrm{APC}}(s)$ for DFIG-based WTs with and without considering the APC.

can be expressed as follows:

$$\Delta\theta_{\mathrm{E}} = -\frac{G_{\mathrm{pll}}(s) + k_{\mathrm{cmd}}k_q G_{\mathrm{q}}(s)}{\left(k_\delta + k_{\mathrm{PEd}}k_q G_{\mathrm{q}}(s)\right)\left(1 - G_{\mathrm{pll}}(s)\right)}\Delta P_e. \tag{26}$$

Furthermore, the inertia transfer function $J_{\mathrm{RPC}}(s)$ when considering the RPC can be expressed as follows:

$$J_{\mathrm{RPC}}(s) = \frac{\omega_1\left(k_\delta + k_{\mathrm{PEd}}k_q G_{\mathrm{q}}(s)\right)\left(1 - G_{\mathrm{pll}}(s)\right)}{s^2\left(G_{\mathrm{pll}}(s) + k_{\mathrm{cmd}}k_q G_{\mathrm{q}}(s)\right)}. \tag{27}$$

B. Impacts of APC and RPC on Inertia

Fig. 13 shows the bode diagram of the inertia transfer function with and without considering the APC based on (13) and (14). The damping coefficient is selected as 0.707 in these cases. As can be seen, the magnitude under the case $\mathrm{BW}_{\mathrm{pll}} = 0.7$ Hz considering the APC is far less than the case $\mathrm{BW}_{\mathrm{pll}} = 1$ Hz without considering the APC. And, even if the PLL bandwidth reduces to 2 Hz, the magnitude of the inertia transfer function without considering the APC is still much larger than the case $\mathrm{BW}_{\mathrm{pll}} = 0.7$ Hz considering the APC. For the phase characteristics, it can be found that the phase under the case with considering the APC decreases from 90° while the phase under the cases without considering APC decreases from 0°, which means that a faster inertial response can be obtained when introducing the APC.

Based on the analysis in Fig. 13, more critical extrapolations can be obtained. First, for the inertia analysis, the APC can be excluded from the electromechanical timescale since a superior inertial response is obtained when removing the APC. Second, the inertia control methods, such as attaching inertia-related reference to the active power reference or the current reference, as shown in Fig. 14, may present striking differences under lower PLL bandwidth, such as $\mathrm{BW}_{\mathrm{pll}} = 2$ Hz or higher. And, revising the current reference will bring in better inertial response performances. Lastly, APC benefits for improving the response speed of the active power. However, insufficient magnitude of the inertia transfer function may result in the response speed becoming less important.

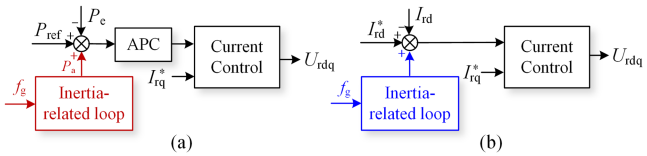

Fig. 14. Inertia control methods by revising references. (a) Revising the active power reference. (b) Revising the current reference.

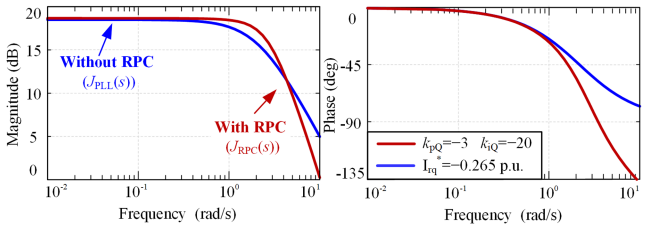

Fig. 15. Bode diagram of inertia transfer function $J_{\rm pll}$(s) and $J_{\rm RPC}$(s) for DFIG-based WTs with and without considering the RPC.

Fig. 15 shows the bode diagram with and without considering the RPC according to (14) and (27). The reactive power reference $Q_{\rm ref}$ in Fig. 1 when adopting the RPC is selected as 0 and the corresponding q-axis rotor current $I_{\rm rq0}$ in the steady state is -0.265 p.u. In other words, the cases in Fig. 15 have the same operation points. And, the PLL parameters are selected as $k_{\rm ppll} = 4.31$ and $k_{\rm ipll} = 9.31$. As can be seen in Fig. 15, the maximum magnitude with and without considering the RPC are the same. The magnitude around 10^0 rad/s considering the RPC is slightly larger than the case without considering the RPC, but the differences still can be tolerated. The situation presents a huge difference in the phase characteristics. The phase under the cases with and without considering the RPC all decreases from 0°, whereas, the phase under the case with considering the RPC finally stables at $-180°$ while the phase under the case without considering the RPC reaches $-90°$. Obviously, the phase when considering the RPC is significantly smaller than the situation without considering the RPC. According to the conclusions obtained in Fig. 6, less phase delay will contribute to a faster inertial response. The inertial response without considering the RPC will be faster than the situation considering the RPC.

Except for the impacts of the phase on the response speed for the inertial response, the differences in the phase characteristics can also be explained from the perspective of damping according to automatic control theories [29]. If the phase differences are explained by the damping, a more critical conclusion in Fig. 15 is that the damping will be greatly reduced when the phase is broadly decreased. As a result, the active power boost during the inertial response will significantly increase. In brief, a larger inertial response can be easily achieved under broad phase reduction. And, this conclusion will be verified by the experiments in the next section.

C. Improved Frequency Support Method

As pointed out in Section IV-B, the APC will weaken the inertial response. When removing the APC, the PLL is no longer required to be tuned to a very low bandwidth for a satisfied

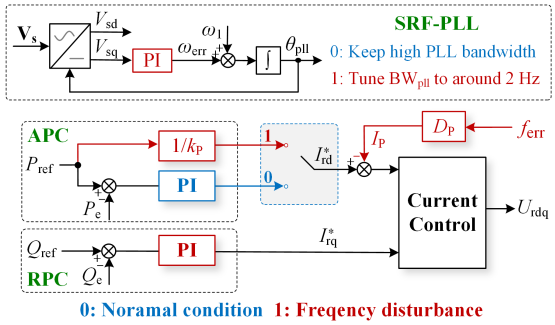

Fig. 16. Control structure of the improved frequency support method for DFIG-based WTs.

inertial response. And, revising the d-axis current reference can obtain a better inertial response performance than revising the power reference The RPC will bring in a significant improvement in the active power boost during the frequency disturbance at the expense of slightly slowing the response speed.

Based on these conclusions, the control structure of the proposed improved frequency support method is shown in Fig. 16. Under normal conditions, the APC and RPC work together for satisfactory performances. And, the PLL usually adopts typical PLL parameters. When the frequency disturbances occur, the bandwidth of the PLL should be tuned to around 2 Hz. Low PLL bandwidth makes the PLL present a long dynamic. Since the RSC control is based on the output phase angle of the PLL, the RSC will correspondingly present a dynamic. Finally, the output active power of the DFIG-based WT will change and the power change satisfies the requirement of inertial response. This is the underlying activation mechanism of the inertial response for the DFIG-based WT.

Furthermore, the APC should be removed and replaced by the d-axis rotor current $I_{\rm rd}{}^*$ for superior inertial response. The relation between the active power and the d-axis rotor current can be derived according to (1) and (2). In the steady state, the q-axis stator voltage $V_{\rm sq}$ equals 0. Then, the d-axis stator flux $\Psi_{\rm sq}$ can also be considered as 0, and (28) can be obtained

$$\Psi_{\rm sd} = -L_{\rm s} I_{\rm sd} + L_{\rm m} I_{\rm rd} = 0. \tag{28}$$

Taking (28) into (2), it yields the following:

$$P_{\rm ref} = V_{\rm sd} I_{\rm sd} = V_{\rm sd} \frac{L_{\rm m}}{L_{\rm s}} I_{\rm rd} = k_{\rm P} I_{\rm rd}^*. \tag{29}$$

The primary frequency regulation capability is also included in the improved frequency support method and represented by the damping coefficient $D_{\rm P}$ in Fig. 16. And, the frequency error $f_{\rm err}$ is provided by the PLL. The damping coefficient $D_{\rm P}$ can be determined by the following:

$$D_{\rm P} = \frac{I_{\rm P}}{f_{\rm err}} = \frac{L_{\rm s}}{L_{\rm m} V_{\rm s}} \frac{P_{\rm P}}{f_{\rm err}} = \frac{2\pi L_{\rm s}}{L_{\rm m} V_{\rm s}} \frac{P_{\rm P}}{\omega_{\rm err}}. \tag{30}$$

Note that the improved frequency support method will not react to the minor frequency derivation by introducing the dead zone. The dead zone for the rate of change of frequency (RoCoF) has a recommended value of 0.05 Hz/s according to the technical rules for connecting wind farms to power systems in China [31].

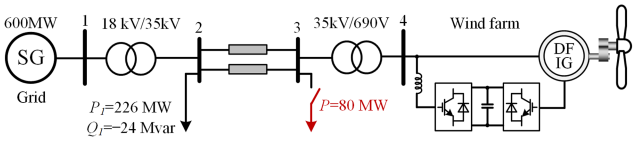

Fig. 17. Configuration of the experimental system.

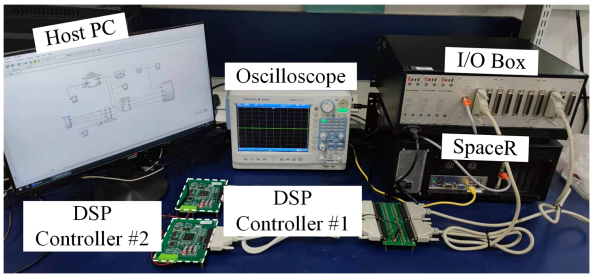

Fig. 18. Photo of the HIL platform.

Therefore, after introducing the dead zone of RoCoF into the proposed method, the DFIG-based WT system can tolerate tiny and frequent disturbances during activation/deactivation.

V. Experimental Verification

To verify the correctness of the analysis results and performances of the proposed method, a wind farm connected to the synchronous generator is established in the hardware-in-loop (HIL) experimental platform, as shown in Fig. 17 [32]. The initial output power of the SG is 100 MW. The wind farm consists of 140 × 1.5 MW DFIG-based WTs and the wind power production is nearly 150 MW. The detailed parameters of a 1.5 MW DFIG-based WT are given in Table III in the Appendix. An 80 MW load is put into the system to mimic the under-frequency disturbances. The reason for the authors choosing the HIL to conduct the frequency-related experiments is that it is very hard to emulate the frequency disturbance in the laboratory scenario. Although the laboratory has the real DFIG-based WT, the capacity of the WT is only 10 kW, making it impossible to change the frequency when compared to the public grid with the capability of several MW. The photo of the HIL platform is shown in Fig. 18. The main circuit topology of the experimental system, including the DFIG-based WT and SG, is developed in SpaceR. The control algorithm is executed in digital signal processing (DSP). The DSP controllers exchange the digital signals and pulsewidth modulation signals with the real-time system through the I/O box.

A. Experiment Results for Impacts of the PLL

Fig. 19 shows the experimental results under the same time constant $T_{\rm pll}$ ($T_{\rm pll} = 0.46$) and without the APC. As can be seen, the active power dynamic under the three cases is similar, but the active power boost when $k_{\rm ipll} = 9.31$ lives up to 0.05 p.u. and is 0.02 p.u. larger than the case when $k_{\rm ipll} = 19.44$. According to the grid codes in China [31], the maximum active power boost is 0.05 p.u. for WTs. Therefore, the inertial response under the case

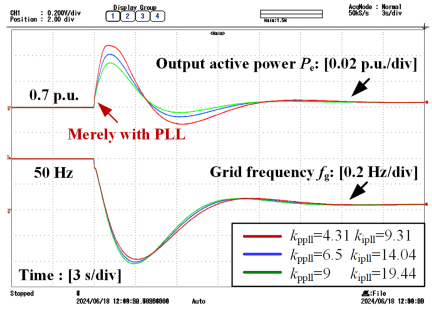

Fig. 19. Inertial response for DFIG-based WTs under the same filter time constant $T_{\rm pll}$ and without the APC.

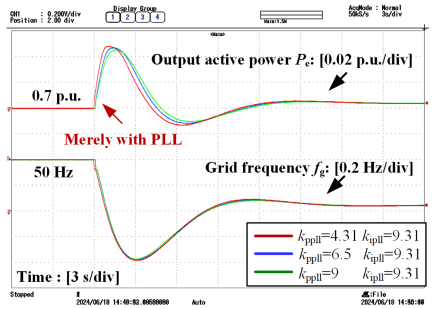

Fig. 20. Inertial response for DFIG-based WTs under the same integral coefficient $k_{\rm ipll}$ and without the APC.

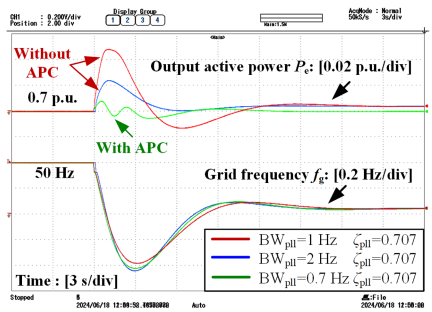

Fig. 21. Inertial response for DFIG-based WTs with and without the APC.

$k_{\rm ipll} = 9.31$ is very significant. And, the RoCoF and maximum frequency excursion when $k_{\rm ipll} = 9.31$ are the smallest.

Fig. 20 shows the experimental results under the same integral coefficient $k_{\rm ipll}$ ($k_{\rm ipll} = 9.31$) and without the APC. As can be seen, the moment reaching the maximum active power when $k_{\rm ppll} = 4.31$ ($T_{\rm pll} = 0.46$) is 0.9 s faster than the case $k_{\rm ppll} = 9$ ($T_{\rm pll} = 0.97$). Besides, the active power boost under the $k_{\rm ppll} = 4.31$ is also slightly larger than other cases. In short, the integral coefficient $k_{\rm ipll}$ proportionally amplifies the magnitude of the power boost while a larger time constant $T_{\rm pll}$ will introduce a significant delay and slightly weaken the power boost during the inertial response. The experimental results are consistent with the analysis in Figs. 6 and 7.

B. Experiment Results for Impacts of APC and RPC

Fig. 21 shows the experimental results with and without the APC. The parameters in this case are the same as the analysis

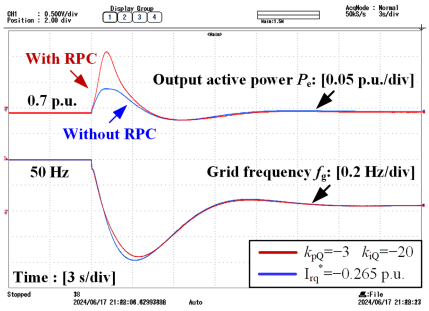

Fig. 22. Inertial response for DFIG-based WTs with and without RPC.

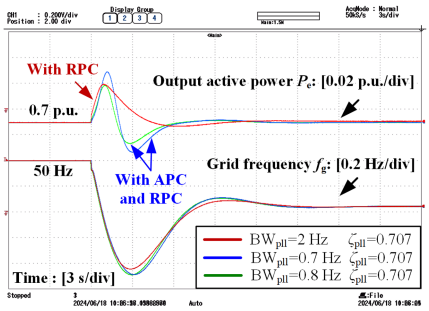

Fig. 23. Comparisons of the inertial response for DFIG-based WTs between the common inertia control method in PLL and the proposed method.

of Fig. 13. As can be seen, when introducing the APC, the active power boost is merely 0.01 p.u, even though the PLL bandwidth reduces to 0.7 Hz. After removing the APC, the active power boost during the inertial response can live up to 0.05 p.u. when the PLL bandwidth raises to 1 Hz. Although the inertial response is weakened when the PLL bandwidth increases to 2 Hz, the power boost also reaches 0.025 p.u., which is still greatly larger than the case introducing the APC. Besides, it should be noted that the response speed when introducing the APC is significantly faster than the situation removing the APC. That is why the APC is required under normal conditions but the APC may be removed during the inertial response. The experimental results are consistent with the analysis for Figs. 13 and 14.

Fig. 22 shows the experimental results with and without RPC. The PLL parameters are all selected as $\mathrm{BW_{pll}} = 1$ Hz and $\zeta_{\mathrm{pll}} = 0.707$ in the two cases. As can be seen, the active power boost under the situation adopting the RPC lives up to 0.11 p.u. while reducing to 0.04 p.u. under the situation without RPC. Besides, the moment to reach the maximum active power without the RPC is 0.2 s faster than the situation with RPC, but the improvement is very limited. The experiment results verify the conclusions obtained in Fig. 15.

C. Experiment Results for the Proposed Method

Fig. 23 compares the inertial response for DFIG-based WT under three cases. The cases with APC and RPC and reducing the PLL bandwidth is the most common inertia control method in PLL. The case with RPC is actually the proposed frequency support method with $D_{\mathrm{P}} = 0$. As can be seen, the active power boost can reach 0.03 p.u. with the proposed method, which is close to the common inertia control method when $\mathrm{BW_{pll}} = 0.7$ Hz. However, the PLL bandwidth under the proposed method only requires to be reduced to 2 Hz, which is significantly larger than the bandwidth with common inertia control under a similar active power boost. Even further reducing the PLL bandwidth to 0.7 Hz, the active power boost reaches 0.04 p.u. but the RoCoF and the maximum frequency excursion under the common inertia control method are significantly larger than the proposed method. Therefore, the inertial performance of the proposed method under the situation that $D_{\mathrm{P}} = 0$ is superior to the common inertia control by reducing the PLL bandwidth to extremely low values.

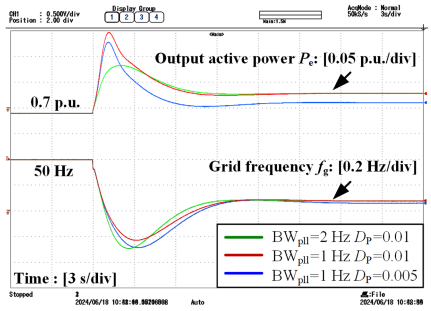

Fig. 24. Inertial response of the improved frequency support method under different parameter configurations for DFIG-based WTs.

Fig. 24 compares the inertial response under different parameter configurations of the proposed frequency support method. As can be seen, after introducing the primary frequency regulation loop, the power boost lives up to 0.09 p.u. when $\mathrm{BW_{pll}} = 2$ Hz and $D_{\mathrm{P}} = 0.01$. The frequency response is much larger when the PLL bandwidth decreases and the damping coefficient D_{P} increases. Compared with the inertial control method by sorely adjusting the PLL bandwidth shown in Fig. 23, the inertial response under the improved frequency control method is significantly raised. Notably, since the frequency response when $\mathrm{BW_{pll}} = 2$ Hz and $D_{\mathrm{P}} = 0.01$ is very striking, the PLL bandwidth can be tuned higher to make a tradeoff between the dynamic performance under normal situations and the inertial response.

VI. Conclusion

This article focuses on examining the effects of APC and RPC on the inertia for DFIG-based WTs. After understanding the significance of the APC and RPC, an improved frequency support method is naturally achieved. The article attempts to change the general understanding that the APC must be considered while the RPC can be neglected in the inertia analysis. The main conclusions can be summarized as follows:

1) For the typical phase motion model by considering the PLL and APC (without RPC), a slight inertial response can be observed even if the PLL bandwidth decreases to 0.7 Hz, as can be proven by the green line in Fig. 21.
2) For the phase motion model by considering the PLL (without APC and RPC), although the structures of various PLLs have some differences, the small-signal models of these PLLs can be represented by the SRF-PLL

or the LPF-SRF-PLL. Specifically, the filter constant $T_{\rm f}$ in the LPF-SRF-PLL poses little impact on the inertia while the integral proportional coefficient $k_{\rm ipll}$ and the filter time constant $T_{\rm pll}$ in PLLs will determine the active power boost and response speed of the inertial response, respectively.

3) For the phase motion model with and without considering the APC, removing the APC significantly improves the inertial response at the sacrifice of decelerating the dynamic performance under normal conditions. However, it is still worth removing the APC since a satisfied inertial response can be obtained and the PLL bandwidth is not required to be tuned to an extremely low value.
4) For the phase motion model by considering the PLL and RPC (without APC), the RPC will greatly strengthen the inertial response while the control parameters of the RPC have little impact on the inertia. More importantly, the phase of the inertia transfer function should be paid more attention for it may also remarkably increase the active power boost during the inertial response.
5) The proposed improved frequency support method can not only provide the inertial response but also the primary frequency regulation capability. Compared with the method of directly reducing the PLL bandwidth to 0.7 Hz, a superior inertial response can be obtained by the proposed method with higher PLL bandwidth.

APPENDIX

TABLE III
PARAMETERS OF A 1.5 MW DFIG-BASED WT

Symbol	Value	Symbol	Value
$P_{\rm N}$	1.5 MW	$R_{\rm r}$	0.016 p.u.
$V_{\rm g}$	690 V	$L_{\rm m}$	2.9 p.u.
$f_{\rm g}$	50 Hz	$L_{\rm ls}$	0.18 p.u.
$U_{\rm dc}$	1200 V	$L_{\rm lr}$	0.16 p.u.
$U_{\rm r\text{-}base}$	2350 V	$C_{\rm dc}$	10000 μF
$I_{\rm s\_base}$	1255 A	$H_{\rm WT}$	4.32 s
$I_{\rm r\_base}$	368 A	$k_{\rm pP}$, $k_{\rm iP}$	0.4, 40
$Z_{\rm b\_base}$	0.3174 Ω	$k_{\rm pQ}$, $k_{\rm iQ}$	−3, −20
$L_{\rm b\_base}$	1.0103 mH	$k_{\rm pi}$, $k_{\rm ii}$	0.6, 8
$R_{\rm s}$	0.023 p.u.	$k_{\rm ppll}$, $k_{\rm ipll}$	60, 1400

REFERENCES

[1] K. Yan, G. Li, R. Zhang, Y. Xu, T. Jiang, and X. Li, "Frequency control and optimal operation of low-inertia power systems with HVDC and renewable energy: A review," *IEEE Trans. Power Syst.*, vol. 39, no. 2, pp. 4279–4295, Mar. 2024.

[2] Y. Zhang, X. Qu, G. Wang, J. Mei, H. H.-C. Iu, and T. Fernando, "A combined bus port impedance based stability criterion for dc distribution power systems," *IEEE Trans. Smart Grid*, vol. 15, no. 5, pp. 4364–4376, Sep. 2024.

[3] Z. He, J. Hu, L. Lin, P. Zeng, and L. Hang, "A generalized dc asymmetrical fault analysis method for MMC-HVDC grids considering metallic return conductors," *IEEE Trans. Power Del.*, vol. 39, no. 5, pp. 2568–2579, Oct. 2024, doi: 10.1109/TPWRD.2024.3400769.

[4] N. Kayedpour, J. D. M. D. Kooning, A. E. Samani, F. Kayedpour, L. Vandevelde, and G. Crevecoeur, "An optimal wind farm operation strategy for the provision of frequency containment reserve incorporating active wake control," *IEEE Trans. Sustain. Energy*, vol. 15, no. 1, pp. 276–289,

[5] W. Si and J. Fang, "Transient stability improvement of grid-forming converters through voltage amplitude regulation and reactive power injection," *IEEE Trans. Power Electron.*, vol. 38, no. 10, pp. 12116–12125, Oct. 2023.

[6] B. Hu, L. Zhan, S. Sahoo, L. Chen, H. Nian, and F. Blaabjerg, "Synchronization stability analysis under ultra-weak grid considering reactive current dynamics," *IEEE Trans. Ind. Electron.*, vol. 71, no. 11, pp. 15220–15223, Nov. 2024, doi: 10.1109/TIE.2024.3370947.

[7] X. He, L. Huang, I. Subotić, V. Häberle, and F. Dörfler, "Quantitative stability conditions for grid-forming converters with complex droop control," *IEEE Trans. Power Electron.*, vol. 39, no. 9, pp. 10834–10852, Sep. 2024.

[8] A. Berrueta, J. Sacristán, J. López, J. L. Rodríguez, A. Ursúa, and P. Sanchis, "Inclusion of a supercapacitor energy storage system in DFIG and full-converter PMSG wind turbines for inertia emulation," *IEEE Trans. Ind. Appl.*, vol. 59, no. 3, pp. 3754–3763, May/Jun. 2023.

[9] D. Yang et al., "Adaptive frequency droop feedback control-based power tracking operation of a DFIG for temporary frequency regulation," *IEEE Trans. Power Syst.*, vol. 39, no. 2, pp. 2682–2692, Mar. 2024.

[10] N. R. Ullah, T. Thiringer, and D. Karlsson, "Temporary primary frequency control support by variable speed wind turbines—Potential and applications," *IEEE Trans. Power Syst.*, vol. 23, no. 2, pp. 601–612, May 2008.

[11] Y. Zhou, D. Zhu, X. Zou, C. He, J. Hu, and Y. Kang, "Adaptive temporary frequency support for DFIG-based wind turbines," *IEEE Trans. Energy Convers.*, vol. 38, no. 3, pp. 1937–1949, Sep. 2023.

[12] A. Berrueta, J. Sacristán, J. López, J. L. Rodríguez, A. Ursúa, and P. Sanchis, "Inclusion of a supercapacitor energy storage system in DFIG and full-converter PMSG wind turbines for inertia emulation," *IEEE Trans. Ind. Appl.*, vol. 59, no. 3, pp. 3754–3763, May/Jun. 2023.

[13] M. Zhang, X. Yuan, and J. Hu, "Inertia and primary frequency provisions of PLL-synchronized VSC HVDC when attached to islanded ac system," *IEEE Trans. Power Syst.*, vol. 33, no. 4, pp. 4179–4188, Jul. 2018.

[14] X. Guo, X. Yuan, D. Zhu, X. Zou, and J. Hu, "Evaluation and optimization of DFIG-based WTs for constant inertia as synchronous generators," *IEEE Trans. Power Electron.*, vol. 39, no. 8, pp. 10453–10464, Aug. 2024.

[15] W. He, X. Yuan, and J. Hu, "Inertia provision and estimation of PLL-based DFIG wind turbines," *IEEE Trans. Power Syst.*, vol. 32, no. 1, pp. 510–521, Jan. 2017.

[16] X. Guo et al., "Dynamic inertia evaluation for type-3 wind turbines based on inertia function," *IEEE J. Emerg. Sel. Topics Circu. Syst.*, vol. 11, no. 1, pp. 28–38, Mar. 2021.

[17] X. Guo, D. Zhu, J. Hu, X. Zou, Y. Kang, and J. M. Guerrero, "Inertial PLL of grid-connected converter for fast frequency support," *CSEE J. Power Energy Syst.*, vol. 9, no. 4, pp. 1594–1599, Jul. 2023.

[18] J. Fang, R. Zhang, H. Li, and Y. Tang, "Frequency derivative-based inertia enhancement by grid-connected power converters with a frequency-locked-loop," *IEEE Trans. Smart Grid*, vol. 10, no. 5, pp. 4918–4927, Sep. 2019.

[19] D. Zhu, X. Guo, B. Tang, J. Hu, X. Zou, and Y. Kang, "Feedforward frequency deviation control in PLL for fast inertial response of DFIG-based wind turbines," *IEEE Trans. Power Electron.*, vol. 39, no. 1, pp. 664–676, Jan. 2024.

[20] L. Harnefors, M. Schweizer, J. Kukkola, M. Routimo, M. Hinkkanen, and X. Wang, "Generic PLL-based grid-forming control," *IEEE Trans. Power Electron.*, vol. 37, no. 2, pp. 1201–1204, Feb. 2022.

[21] Y. He, X. Wang, X. Ruan, D. Pan, and K. Qin, "Hybrid active damping combining capacitor current feedback and point of common coupling voltage feedforward for LCL-type grid-connected inverter," *IEEE Trans. Power Electron.*, vol. 36, no. 2, pp. 2373–2383, Feb. 2021.

[22] L. Sun and X. Zhao, "Impacts of phase-locked loop and reactive power control on inertia provision by DFIG wind turbine," *IEEE Trans. Energy Convers.*, vol. 37, no. 1, pp. 109–119, Mar. 2022.

[23] Y. Yoo, S. Song, J. Suh, J.-H. Kim, R.-J. Park, and S. Jung, "Adaptive response method for communication failures of hierarchical reactive power control in wind farms," *IEEE Trans. Sustain. Energy*, vol. 13, no. 4, pp. 2343–2352, Oct. 2022.

[24] M. N. S. K. Shabbir, X. Liang, and S. Chakrabarti, "A hierarchical voltage control scheme for wind power plants through enhanced reactive power support," *IEEE Trans. Ind. Appl.*, vol. 58, no. 5, pp. 5776–5791, Sep./Oct. 2022.

[25] X. Li and H. Lin, "A design method of phase-locked loop for grid-connected converters considering the influence of current loops in weak grid," *IEEE J. Emerg, Sel. Topics Power Electron.*, vol. 8, no. 3, pp. 2420–2429, Sep. 2020.

[26] P. Rodriguez, J. Pou, J. Bergas, J. I. Candela, R. P. Burgos, and D. Boroyevich, "Decoupled double synchronous reference frame PLL for power converters control," *IEEE Trans. Power Electron.*, vol. 22, no. 2,

[27] S. Golestan, M. Monfared, F. D. Freijedo, and J. M. Guerrero, "Dynamics assessment of advanced single-phase PLL structures," *IEEE Trans. Ind. Electron.*, vol. 60, no. 6, pp. 2167–2177, Jun. 2013.
[28] Y. Zhou et al., "Magnitude-phase characteristics analysis of inertia for DFIG-based wind turbines," *IEEE Trans. Power Electron.*, vol. 39, no. 10, pp. 12336–12348, Oct. 2024, doi: 10.1109/TPEL.2024.3410294.
[29] G. Ellis, *Control System Design Guide: A Practical Guide*. San Diego, CA, USA: Elsevier, 2004.
[30] G. Abad, J. Lopez, M. A. Rodriguez, L. Marroyo, and G. Iwanski, *Doubly Fed Induction Machine Modeling and Control for Wind Energy Generation Applications*. Hoboken, NJ, USA: Wiley, 2011.
[31] Technical Specification for connecting wind farm to power system—Part 1: Onshore Wind Power, GB/T 19963.1-2021, 2021.
[32] X. Guo et al., "Analysis and enhancement of active power transfer capability for DFIG-based WTs in very weak grid," *IEEE J. Emerg, Sel. Topics Power Electron.*, vol. 10, no. 4, pp. 3895–3906, Aug. 2022.

Xiang Guo (Member, IEEE) was born in Jiangsu, China, in 1995. He received the Ph.D. degree in electrical engineering from the Huazhong University of Science and Technology, Wuhan, China, in 2022.

He is currently an Associate Professor with the School of Electrical Engineering, China University of Mining and Technology, Xuzhou, China. His current research interests include renewable energy technology, frequency control, stability and power quality of converter-based power systems.

Qingbo Tang was born in Hunan, China, in 1994. He received the B.S. and M.S. degrees in electrical engineering from the Huazhong University of Science and Technology, Wuhan, China, in 2017 and 2020, respectively.

He is currently working for the Hubei Key Laboratory of Marine Electromagnetic Detection and Control, Wuhan. His current research interests include renewable energy control technology and power electronic converters.

Donghai Zhu (Senior Member, IEEE) was born in Anhui, China. He received the Ph.D. degree in electrical engineering from the Huazhong University of Science and Technology, Wuhan, China, in 2018.

He is currently an Associate Professor with the School of Electrical and Electronic Engineering, Huazhong University of Science and Technology, Wuhan. His current research interests include renewable power generation system and power electronic converters.

Dr. Zhu was selected for the National Postdoctoral Program for Innovative Talents in 2018. He was a recipient of IEEE TRANSACTIONS ON ENERGY CONVERSION Best Paper Award in 2019 and the Excellent Doctoral Dissertation Award of China Power Supply Society in 2022. He currently serves as the Associate Editor for IEEE TRANSACTIONS ON INDUSTRY APPLICATIONS, *IET Renewable Power Generation*, and *Protection and Control of Modern Power Systems*.

Yini Zhou (Student Member, IEEE) was born in Hubei, China, in 1998. She received the B.S. degree in electrical engineering from the Wuhan University of Technology, Wuhan, China, in 2020. She is currently working toward the Ph.D. degree in the School of Electrical and Electronic Engineering, Huazhong University of Science and Technology, Wuhan.

Her current research interests include renewable energy technology, including the modeling, analysis, and control of DFIG-based wind turbines' inertia.

Xudong Zou (Member, IEEE) was born in Hunan, China, in 1974. He received the B.S., M.S., and Ph.D. degrees in electrical engineering from the Huazhong University of Science and Technology, Wuhan, China, in 1997, 2000, and 2005, respectively.

Since 2005, he has been a Faculty Member with the Huazhong University of Science and Technology, where he is currently a Full Professor with the School of Electrical and Electronic Engineering. His current research interests include power electronic converters, renewable energy generation system, and flywheel energy storage. Dr. Zou was a recipient of IEEE TRANSACTIONS ON ENERGY CONVERSION Best Paper Award in 2019.

Jiabing Hu (Senior Member, IEEE) received the B.Eng. and Ph.D. degrees in electrical engineering from College of Electrical Engineering, Zhejiang University, Hangzhou, China, in 2004 and 2009, respectively.

He is currently a Professor with the School of Electrical and Electronic Engineering, Huazhong University of Science and Technology, Wuhan, China. His current research interests include grid-integration of large-scale renewables, and modeling, analysis and control of power electronized power systems.

Dr. Hu serves as an Editor of IEEE TRANSACTIONS ON ENERGY CONVERSION, an Associate Editor of *IET Renewable Power Generation*. He is the Co-Convener of IEC SC8A JWG5. He is the IET Fellow.

Yong Kang (Fellow, IEEE) was born in Hubei, China, in 1965. He received the B.E., M.E., and Ph.D. degrees in electrical engineering from the Huazhong University of Science and Technology, Wuhan, China, in 1988, 1991, and 1994, respectively.

Since 1994, he has been a Faculty Member with the Huazhong University of Science and Technology, where he is currently a Full Professor with the School of Electrical and Electronic Engineering. His research interests include the power electronic converters, ac drivers, and renewable energy generation systems.

Dr. Kang was a recipient of the Delta Scholar Award from the Delta Environmental and Educational Foundation in 2005, and supported by the Program for New Century Excellent Talents in University from the Chinese Ministry of Education in 2004. In 2017, he was appointed as the Chief Scientist of the National Key R&D Program of China. He was a recipient of the highly prestigious China National Science and Technology Award in 2019.